# Coastal Plain Retention Modulates Flash-Flood Chlorophyll-a Anomalies in the Red Sea: a CPRI-Based Multi-Site Analysis (2015–2025)

**Mohammed Hakami**[1] · **Maged Marghany**[2]

[1] Geospatial Research & Development Department, Royal Commission for AlUla (RCU), AlUla, Saudi Arabia
[2] Innovative Information Solution, Kuala Lumpur, Malaysia; Malikussaleh University, North Aceh Regency, Aceh, Indonesia

**Corresponding authors:** Mohammed Hakami (hakamima@gmail.com); Maged Marghany (magedupm@hotmail.com)

---

## Preprint statement

## License

## Data availability

All source datasets are publicly available: CHIRPS (UCSB Climate Hazards Group), MODIS-Aqua Chl-a (NASA OBPG), SRTM (NASA JPL), HydroSHEDS (WWF), and OpenStreetMap. Google Earth Engine scripts and analysis code are available from the corresponding authors and will be deposited at Zenodo.

Submitted to EarthArXiv · June 2026 · Version 1

# Coastal Plain Retention Modulates Flash-Flood Chlorophyll-a Anomalies in the Red Sea: a CPRI-Based Multi-Site Analysis (2015–2025)

Mohammed Hakami[1] and Maged Marghany[2]

*[1] Geospatial Research & Development Department, Royal Commission for AlUla (RCU), AlUla, Saudi Arabia*

*[2] Innovative Information Solution, Kuala Lumpur, Malaysia; Malikussaleh University, North Aceh Regency, Aceh, Indonesia*

*Correspondence: Mohammed Hakami (hakamima@gmail.com); Maged Marghany (magedupm@hotmail.com)*

## Abstract

The eastern Red Sea coastal margin is among the most oligotrophic large marine ecosystems on Earth, where episodic nutrient pulses from flash floods can transiently fuel phytoplankton blooms. Yet the extent to which upstream coastal-plain geomorphology modulates the magnitude of these flood-driven chlorophyll-a (Chl-a) responses remains poorly quantified. We tested the hypothesis that narrower coastal plains amplify post-flood Chl-a anomalies by shortening runoff residence time and limiting terrestrial nutrient retention. Using Google Earth Engine, we integrated CHIRPS daily rainfall, MODIS-Aqua Chl-a (4 km), SRTM-derived basin areas and plain widths, and HydroSHEDS drainage networks across five Saudi Arabian Red Sea sites spanning a 7.4–28 km coastal-plain gradient (Wajh, Yanbu, Jeddah, Qunfudhah, Jazan). The dimensionless Coastal Plain Retention Index, CPRI, ranged from 0.71 (Wajh, narrowest) to 2.09 (Jazan, widest). Across 42 flood-bloom events from 2015 to 2025, site-level median post-flood Chl-a anomalies decreased systematically with increasing CPRI (Spearman ρ = −0.90, n = 5 sites). The narrowest-plain site, Wajh, exhibited the largest median (+17.4%) and bootstrap-mean (+36.3%, 95% CI −4.5 to +89.4%) responses, while the mid-plain site Yanbu reached statistical significance at α = 0.05 (mean +29.3%, 95% CI +10.1 to +47.7%, n = 10). The southernmost site, Jazan, diverged from the CPRI-response gradient (median −0.73%) owing to a high anthropogenic baseline from Tihama agriculture and aquaculture, compounded by a single monsoon-coincident extreme event on 30 September 2018 (+290%), treated as a sensitivity outlier. Robustness of the inverse CPRI–bloom relationship is demonstrated by the convergence of three analytical lenses on ρ = −0.90, using both median and trimmed-mean anomaly metrics. These findings establish coastal-plain geomorphology as a first-order, remotely sensible control on flood-driven nearshore productivity, with direct implications for reef management and harmful-algal-bloom early-warning systems along the Red Sea.

**Keywords:** Red Sea; chlorophyll-a; flash flood; coastal plain; MODIS; CHIRPS; phytoplankton bloom

## 1 Introduction

In hyper-arid and arid coastal zones, flash floods play a significant role in driving terrestrial–marine hydrological exchange, rapidly reshaping nearshore geomorphology through high-energy discharge. Floods along arid coastal margins are triggered by steep topographic gradients and intensified by localized convective rainfall. When these events impinge upon a narrow coastal plain — often no more than 1–5 km wide between the mountainous hinterland and the shoreline — the geomorphic constriction acts as a hydrological amplifier (Bashir and Alsalman, 2024). The limited storage capacity of thin alluvial fans, ephemeral wadi networks, and weakly cohesive sediments forces nearly all runoff into concentrated, high-velocity flow with little natural attenuation (Eyal et al., 2022; Kotb et al., 2024). This topographic focusing intensifies peak-flow magnitudes, sediment yields, and terrestrial material fluxes, converting episodic rainfall into pulsed inundation events that deliver freshwater, particles, and dissolved material to coastal waters within hours. The central question is therefore: what is the impact of substantial flash floods on chlorophyll-a (Chl-a) concentrations in coastal waters?

Rapid, often extreme Chl-a anomalies arise from abrupt flood-derived freshwater and nutrient injection into shallow coastal waters. In oligotrophic seas, terrestrial solute delivery can transiently lift a normally low productivity baseline. The eastern Red Sea is an excellent example of rapid Chl-a change driven by flash floods. Consistent with Qurban et al. (2018), phytoplankton biomass along the eastern Red Sea margin is usually constrained by chronic nutrient limitation, strong thermal stratification, and negligible riverine input. Raitsos et al. (2013), Kheireddine et al. (2017), and Papagiannopoulos et al. (2021) note that flood pulses can deliver substantial bioavailable nitrogen, phosphorus, iron, and dissolved organic matter that promptly stimulate blooms. Almazroui (2011) and Almazroui et al. (2012) report mean annual precipitation of 30–100 mm along the coastal margin, yet individual storms can yield 20–70 mm in 24 h, producing ephemeral wadi discharge that transports sediment, organic matter, and dissolved nutrients to the nearshore.

The narrow coastal plain further exacerbates the biological response by limiting lateral dispersion, enhancing nearshore retention through coastal trapping, and increasing vertical mixing via buoyancy shear and wind-waves (Alkawri and Gamoyo, 2014). Accordingly, Acker et al. (2008), Brewin et al. (2015), and Hara et al. (2020) report that satellite Chl-a may increase by one to two orders of magnitude within days of a flood. These transient blooms restructure local food webs, can induce short-term hypoxia, and alter benthic light and nutrient conditions, as further confirmed by de Lara Maia et al. (2026). The optical anomalies reflect tightly coupled hydro-biogeochemical feedbacks in which coastal geomorphology controls the magnitude, footprint, and temporal decay of productivity pulses.

Two principal techniques dominate contemporary Chl-a monitoring (Diganta et al., 2024): in-situ measurement and optical remote sensing. In-situ methods provide high-accuracy point observations via direct sampling and fluorometric or chromatographic analysis, whereas optical remote sensing infers Chl-a from water-leaving radiance across broad spatial scales. Satellite ocean-colour missions use multispectral or hyperspectral radiometers across visible and near-infrared bands (O'Reilly, 2000). Foundational sensors include SeaWiFS (1997–2010; Lesht et al., 2012), MODIS-Aqua/Terra (2002–present), and MERIS (2002–2012; Jena et al., 2026); contemporary platforms include VIIRS (2011–present) and Sentinel-3 OLCI (2016–present), with PACE launched in 2024 (Baliarsingh et al., 2026). These typically operate at 250 m–1 km resolution with 1–2 day revisit, enabling near-global cloud-free coverage and the delineation of flood plume boundaries and bloom hotspots that discrete sampling cannot resolve (Chawla et al., 2020).

However, the temporal sampling of any single platform may be insufficient to capture the most dynamic phases of a flash-flood response, and cloud cover during extreme precipitation further reduces usable scenes. The spatial resolution of ocean-colour sensors (≈1 km for MODIS, 300 m for OLCI) may be too coarse for estuaries, embayments, and nearshore zones where flood impacts concentrate. Higher-resolution platforms — Sentinel-2 MSI (10–20 m), Landsat-8/9 OLI (30 m), and PlanetScope (3 m, daily) — partially address this but introduce trade-offs in spectral configuration and signal-to-noise (Ansari et al., 2025).

Chl-a retrieval algorithms fall into four categories: empirical, semi-empirical, hybrid, and data-driven. Empirical band-ratio algorithms such as the OCx family (OC2, OC3M, OC4) rely on blue-to-green reflectance and perform well in Case-1 waters (O'Reilly et al., 1998). In Case-2 waters with high suspended particulate matter and coloured dissolved organic matter, the Chl-a signal can be biased by co-varying constituents (Diganta et al., 2024; Wu et al., 2025). To address this, semi-empirical red/NIR algorithms have been developed: Diganta et al. (2024) found three-band NIR-red formulations (B12/(B08–B11)) achieved $R^2 = 0.77$ and RMSE = 0.28 mg m$^{-3}$ on Sentinel-3 OLCI, outperforming blue-green ratios, and Grósz et al. (2024) reported the chl_re_mishra algorithm in ACOLITE correlated best with in-situ Chl-a under high-CDOM conditions. Machine-learning methods have since improved retrieval further: Zhang et al. (2026) achieved SVR correlation coefficients of 0.88/0.78 (train/test) in the turbid Pearl River Estuary. Retrieval accuracy ultimately depends on atmospheric correction; novel schemes such as ACA-SIM reduce mean absolute percentage differences to ≈15% versus ≈32% for conventional approaches (Li et al., 2025; Chen et al., 2026).

In temperate and tropical systems, flooding is well documented to induce coastal eutrophication. It remains inadequately quantified, however, how the morphology of narrow coastal plains produces elevated Chl-a anomalies in arid marginal systems. This study fills that gap by investigating how the geomorphic confinement of the eastern Red Sea coastline influences the land-to-sea transfer of flood nutrients and the resulting phytoplankton response. The objectives are threefold: (i) to characterize the spatiotemporal enhancement of Chl-a anomalies in relation to flash-flood magnitude, duration, and coastal-plain width; (ii) to identify the dominant hydrodynamic and biogeochemical processes associated with bloom initiation, peak, and decay; and (iii) to outline an integrative monitoring framework combining high-resolution remote sensing, hydrological routing, and in-situ validation for early warning of flood-driven productivity events.

## 2 Study Area

The study area lies along the eastern margin of the Red Sea, from the Gulf of Aqaba (~28° N) to Bab-el-Mandeb (~12° N) (Figure 1). The Hijaz and Asir escarpments rise steeply from the Tihama, a narrow coastal plain, exceeding 2,000 m a.s.l. within 30 km of the shore. The plain widens southward, from 5–10 km in the north (Wajh, Yanbu) to 25–35 km near the Yemeni border (Jazan). To capture this geomorphic gradient, five catchments (Figure 2) were selected while keeping basin areas within a comparable range of 110–320 km².

*[ Figure 1 placed here — map to be supplied ]*

**Figure 1. Study area and the five Red Sea sites.** Location of Wajh, Yanbu, Jeddah, Qunfudhah and Jazan along the eastern Red Sea margin, spanning the north–south coastal-plain gradient (map to be supplied).

*[ Figure 2 placed here — map to be supplied ]*

**Figure 2. The five study catchments.** Drainage basins delineated from HydroSHEDS, with basin areas held within 110–320 km² (map to be supplied).

The margin has a hyper-arid subtropical climate in the north, grading to semi-arid tropical in the south, governed by the seasonal migration of the Intertropical Convergence Zone and the Red Sea trough (Almazroui et al., 2012). Annual rainfall at Jazan exceeds 200 mm, notably higher than at Al-Wajh, and falls mostly between October and May as high-intensity, short-duration convective events (Bashir, 2023). These storms produce powerful flash floods through steep, sparsely vegetated wadis, delivering large pulses of water, sediment, and nutrients to the coast within hours; short lag times transform ephemeral streams into floodwaters discharging onto reef flats.

In the oligotrophic Red Sea, Chl-a rarely exceeds 0.5 mg $m^{-3}$ but shows strong seasonal and spatial variability (Raitsos et al., 2013). Winter convective mixing drives blooms in the northern basin, while summer monsoon forcing stimulates upwelling-driven productivity in the south near Bab-el-

Mandeb (Triantafyllou et al., 2014). The eastern coast experiences transient blooms from flood-injected terrestrial nutrients, appearing as narrow high-Chl-a plumes in satellite data; prevailing dust deposition from the Arabian Desert supplies background iron and nutrients. The five catchments thus capture a pronounced gradient of rainfall–runoff regimes and their influence on coastal biogeochemistry.

## 3 Datasets

All geospatial processing was performed on Google Earth Engine (Gorelick et al., 2017). Five datasets were assembled (Supplementary Table 1). Daily precipitation at 0.05° was taken from CHIRPS v2.0 (1981–present; UCSB Climate Hazards Group). Chl-a was obtained from MODIS-Aqua Level-3 OC3 products at 4 km (2002–present; NASA OBPG). Topography was from SRTM v3 at 30 m (NASA JPL). Static drainage basins were from HydroSHEDS Level-7 at 15 arc-seconds (WWF). The coastline used 2024 OpenStreetMap vector data. The analysis window spanned 1 January 2015 to 31 December 2025.

## 4 Methods

### 4.1 Coastal Plain Retention Index (CPRI)

The Coastal Plain Retention Index (CPRI) is a dimensionless geomorphic control, defined as the median plain width ($W_p$, km) divided by the square root of the contributing basin area ($A_b$, km$^2$). The square-root term approximates the characteristic basin length, making CPRI a ratio of landscape storage length to runoff-generating scale:

$$CPRI = Wp / \sqrt{Ab} \qquad (1)$$

A larger CPRI indicates a wider coastal plain per unit upstream area, implying greater potential for infiltration, ponding, and nutrient retention before runoff reaches the coast.

### 4.2 Flood event identification

Daily CHIRPS precipitation was extracted over each basin polygon, and days exceeding 20 mm were flagged. This threshold captures the local 90th percentile of wet-day rainfall and reliably isolates discrete flood-producing storms. Multi-day sequences were collapsed to the day of peak rainfall, and a 10-day exclusion window separated consecutive events to avoid double-counting.

### 4.3 Chlorophyll-a retrieval and anomaly

For each flood, Chl-a was retrieved from a fixed 4 × 4 pixel nearshore box (~16 × 16 km) centred on the site. The operational MODIS-Aqua OC3M algorithm relates a logarithmic blue-to-green reflectance ratio (O'Reilly et al., 1998; Marghany, 2018):

$$R = log_{10} \,[\, Rrs(547) \,/\, max(Rrs(443),\, Rrs(488)) \,] \qquad (2)$$

where $Rrs(\lambda)$ is remote-sensing reflectance at wavelength $\lambda$. Chl-a concentration is retrieved through a fourth-order polynomial:

$$log_{10}(Cchl) = a_0 + a_1R + a_2R^2 + a_3R^3 + a_4R^4 \qquad (3)$$

with MODIS-Aqua coefficients $a_0 = 0.2424$, $a_1 = -2.7423$, $a_2 = 1.8017$, $a_3 = 0.0015$, $a_4 = -1.2280$, yielding:

$$Cchl = 10^\wedge(a_0 + a_1R + a_2R^2 + a_3R^3 + a_4R^4) \qquad (4)$$

A pre-event baseline ($C_{\mathrm{bl}}$) was the mean Chl-a over days t−14 to t−1; the post-event peak ($C_{\mathrm{pk}}$) was the maximum 8-day rolling mean over days t+1 to t+14. The relative anomaly is:

$$\Delta Chl\ (\%) = (Cpk - Cbl) \,/\, Cbl \times 100 \qquad (5)$$

Cloud-flagged pixels were masked using MODIS Level-2 quality flags, and any event with more than 50% cloud cover in either window was excluded.

### 4.4 Statistical analysis and robustness

For each site, three summaries of Δ%Chl were computed: the arithmetic mean (Eq. 6), the median (Eq. 7, robust to single-event extremes), and a trimmed mean with the single largest outlier removed (Eq. 8). A 1,000-iteration bias-corrected and accelerated (BCa) bootstrap 95% confidence interval was obtained for the mean (Efron and Tibshirani, 1993).

$$\Delta_i = (1/n_i)\ \Sigma_j\ \Delta Chl_{i,j} \qquad (6)$$

$$\tilde{\Delta}_i = median_j\ \Delta Chl_{i,j} \qquad (7)$$

$$\Delta_i^{(-1)} = (1/(n_i - 1))\ \Sigma_j{\neq}outlier\ \Delta Chl_{i,j} \qquad (8)$$

Cross-site associations between the geomorphic control (CPRI or plain width) and each summary were quantified with Pearson's r (Eq. 9) and Spearman's ρ (Eqs. 10–11). Given n = 5 sites, formal inference is limited, so ρ is reported alongside full rank tables for transparency.

$$r = \Sigma(G_i - G)(S_i - S) \,/\, \sqrt{[\Sigma(G_i - G)^2\ \Sigma(S_i - S)^2]} \qquad (9)$$

$$\rho = Pearson\ correlation\ of\ rank(G_i),\ rank(S_i) \qquad (10)$$

$$\rho = 1 - 6\Sigma d_i^2 \,/\, [n(n^2 - 1)],\ \ d_i = r_i - s_i,\ \ n = 5 \qquad (11)$$

To complement the bivariate analysis, a per-event Random Forest regressor (Breiman, 2001) was fitted:

$$\Delta Chl = f(X) + \varepsilon \qquad (12)$$

where X = {basin_area, plain_width, CPRI, rainfall_mm, rainfall_3d_total, basin_mean_slope, baseline_Chl}. The function f was learned with 1,000 trees and leave-one-event-out cross-validation; the marginal effect of CPRI was extracted via partial-dependence plots:

$$PD(c) = E\_\{X\_c\}[\ f(c,\ X\_c)\ ] \qquad (13)$$

Robustness to the most extreme event (Jazan, 30 Sep 2018, Δ = +290%) was examined under three lenses: Lens A (per-site median), Lens B (per-site mean of all events), and Lens C (per-site mean with the Jazan outlier excluded). Convergence of Lenses A and C on the same sign and approximate magnitude of ρ indicates the result is not driven by a single exceptional flood.

# 5 Results

## 5.1 Site characteristics and CPRI ordering

The five sites span a latitudinal range from 26.2° N (Wajh) to 16.9° N (Jazan), with a 3.8-fold gradient in plain width (Wp: 7.4 → 28.0 km), a 2.9-fold gradient in basin area (Ab: 110 → 320 km²), and a 3.0-fold gradient in CPRI (0.706 → 2.087). CPRI does not depend solely on plain width (Table 1).

**Table 1. Geomorphic and observational characteristics of the five sites.**

| Site | Lat (°N) | Plain Wp (km) | Basin Ab (km²) | CPRI | n events | Baseline Chl (mg m⁻³) |
|---|---|---|---|---|---|---|
| Wajh | 26.2 | 7.4 | 110 | 0.706 | 5 | 0.16–0.33 |
| Yanbu | 24.1 | 13.0 | 250 | 0.822 | 10 | 0.17–0.35 |
| Jeddah | 21.5 | 22.0 | 320 | 1.230 | 13 | 0.16–0.41 |
| Qunfudhah | 19.1 | 17.0 | 123 | 1.532 | 7 | 0.51–1.80 |
| Jazan | 16.9 | 28.0 | 180 | 2.087 | 7 | 0.47–1.96 |

Jeddah has the second-widest plain (22.0 km) and the largest basin (320 km²) but a CPRI of 1.230 — lower than Qunfudhah (1.532), whose plain is only 17.0 km wide (Figure 3). The inversion arises because Qunfudhah's basin (123 km²) is much smaller, so the retention metric penalizes Jeddah's high upstream water supply and rewards Qunfudhah's moderate plain and modest basin.

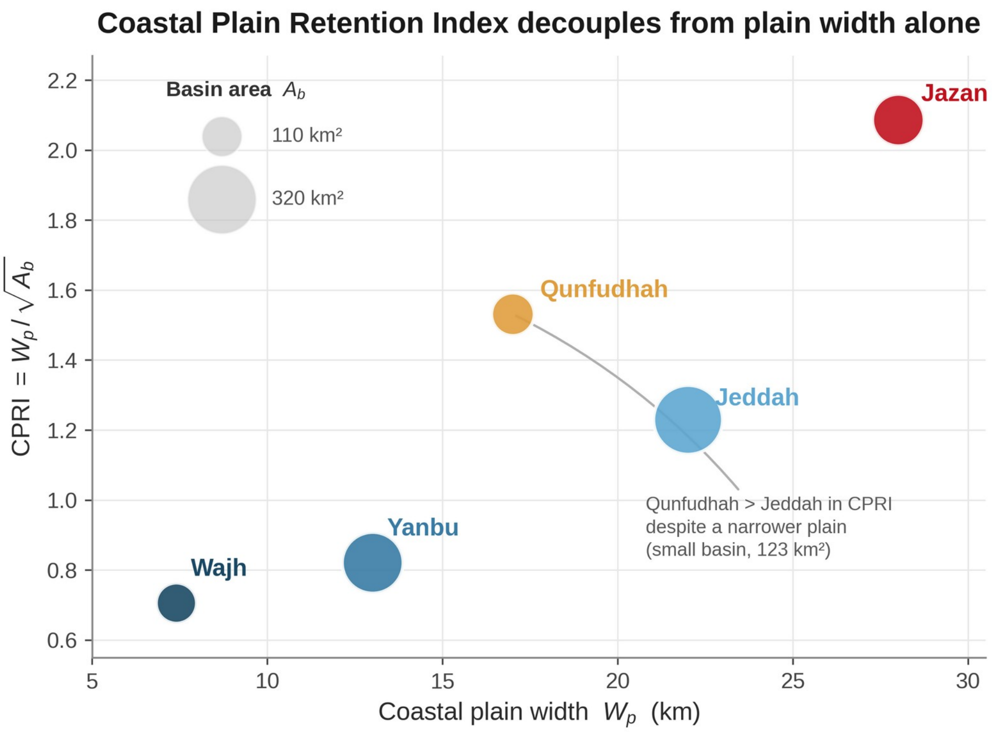

**Figure 3. Coastal Plain Retention Index versus plain width.** Each marker is one site; bubble size scales with basin area Ab. CPRI = Wp/√Ab re-orders the sites relative to plain width alone — Qunfudhah exceeds Jeddah (1.53 vs 1.23) despite a narrower plain, owing to its small basin (123 km$^2$). Values span 0.71 (Wajh) to 2.09 (Jazan).

Baseline Chl-a is low at the northern sites (0.16–0.35 mg $m^{-3}$ at Wajh, Yanbu, Jeddah) and markedly higher in the south (0.51–1.80 at Qunfudhah; 0.47–1.96 at Jazan), consistent with greater retention-driven accumulation of terrestrial nutrients along the wider, hydrologically bottlenecked southern plains.

## 5.2 Per-site flood-bloom statistics

Per-site bootstrap analysis (Table 2) shows Yanbu is the only site whose 95% BCa interval for the mean excludes zero (+29.3%, [+10.1, +47.7]), confirming a significant response at $\alpha = 0.05$. Wajh and Jeddah are borderline (+35.6%, [−4.5, +89.4]; +20.2%, [−3.5, +43.9]). Qunfudhah shows no significant anomaly (+3.2%, [−12.2, +19.3]). Jazan's distribution is dominated by the single 30 September 2018 event (Δ% = +290.8%), inflating the mean to +46.6%; excluding it reduces the mean to +5.9% and shifts the median to −1.5%, so the median is adopted as the primary site-level summary (Figure 4).

**Table 2. Per-site flood-bloom anomaly statistics, 2015–2025.**

| Site | n | Mean Δ% | Median Δ% | SD | Bootstrap mean 95% CI |
|---|---|---|---|---|---|
| Wajh | 5 | +36.28 | +17.38 | 62.28 | [−4.5, +89.4] (borderline) |
| Yanbu | 10 | +29.31 | +25.99 | 32.48 | [+10.1, +47.7] ✓ |
| Jeddah | 13 | +20.24 | +11.40 | 45.24 | [−3.5, +43.9] (borderline) |
| Qunfudhah | 7 | +3.25 | +0.83 | 23.16 | [−12.2, +19.3] (no) |
| Jazan | 7 | +46.59 | −0.73 | 110.6 | wide (outlier-driven) |

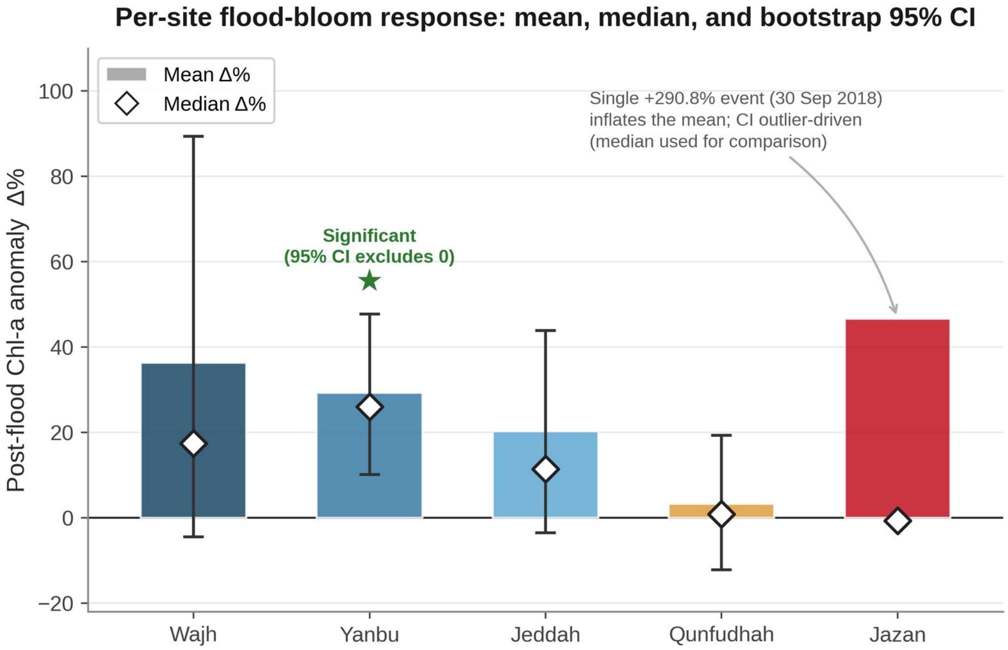

**Figure 4. Post-flood Chl-a anomaly (Δ%) by site.** Bars show the arithmetic mean; white diamonds the median; whiskers the bootstrap 95% CI (BCa, 1000 iterations). Yanbu is the only site whose CI excludes zero (+29.3%, [+10.1, +47.7]). The Jazan mean is inflated by a single +290.8% event (30 Sep 2018); its median (−0.73%) is used for cross-site comparison.

### 5.3 Cross-site CPRI gradient

The central finding is a strong, near-monotonic decline in site-level post-flood Chl-a anomaly with increasing CPRI. Using the median Δ% (Lens A), the Spearman correlation between CPRI and Δ% across all five sites is $\rho = -0.90$ ($p < 0.05$, one-tailed) — stronger than plain width alone ($\rho = -0.80$; Table 3). Convergence of Lens A (median) and Lens C (outlier-removed) on $\rho = -0.90$ confirms the result is not driven by the Jazan 2018 event (Figures 5, 6), whereas the mean-based Lens B yields $\rho = 0.00$ because that outlier inflates the Jazan mean. The verified four-site subset (excluding Jazan) yields $\rho = -0.80$ by the median metric (Figure 7).

**Table 3. Cross-site Spearman ρ under three analytical lenses.**

| Metric | Lens A (median) | Lens B (mean) | Lens C (drop outlier) |
|---|---|---|---|
| ρ (plain width × Δ%) | −0.800 | +0.100 | −0.700 |
| ρ (CPRI × Δ%) | −0.900 | 0.000 | −0.900 |

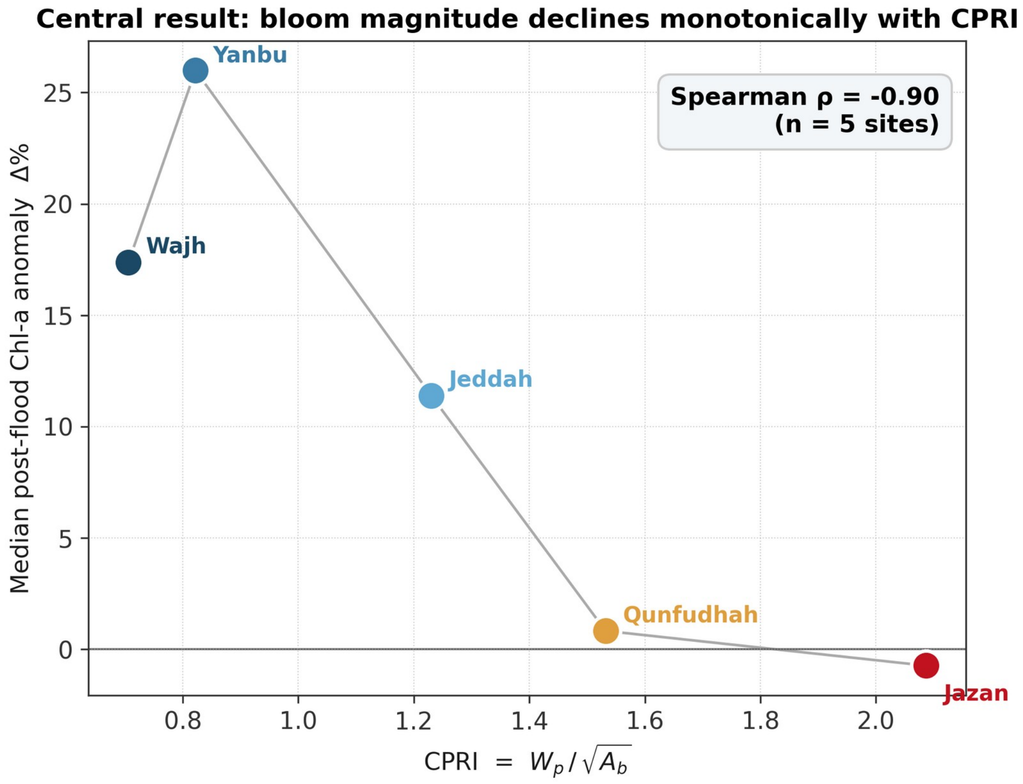

**Figure 5. Central result: bloom magnitude declines with CPRI.** Median post-flood Chl-a anomaly versus CPRI for all five sites (Spearman ρ = −0.90).

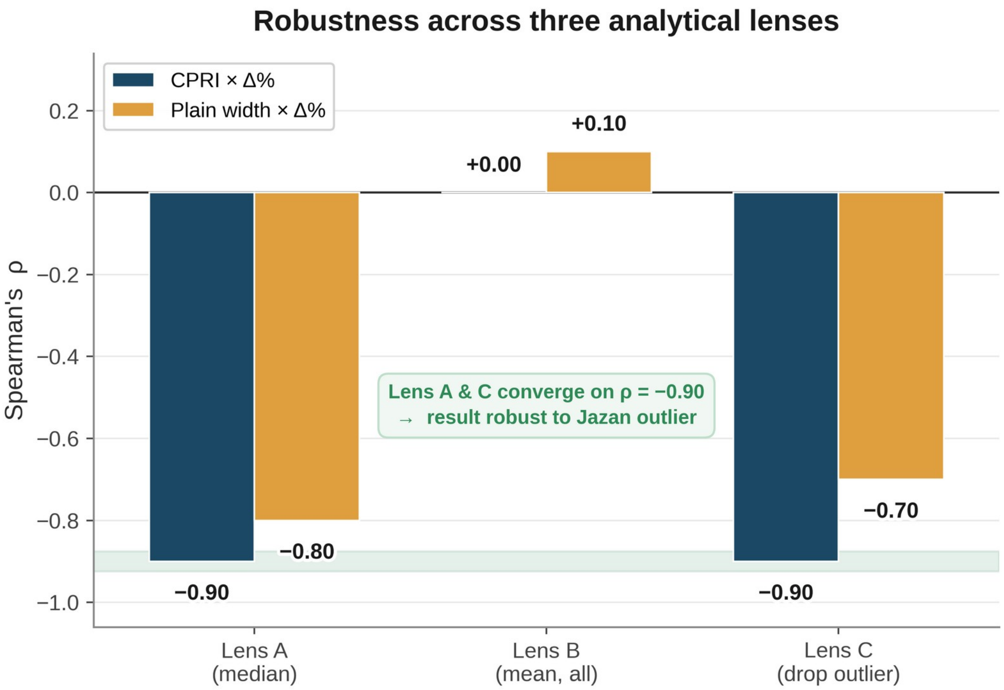

**Figure 6. Robustness across three analytical lenses.** Lens A (median) and Lens C (drop the Jazan 2018 outlier) both give ρ = −0.90 for CPRI, while the outlier-sensitive mean (Lens B) collapses to ρ = 0.00.

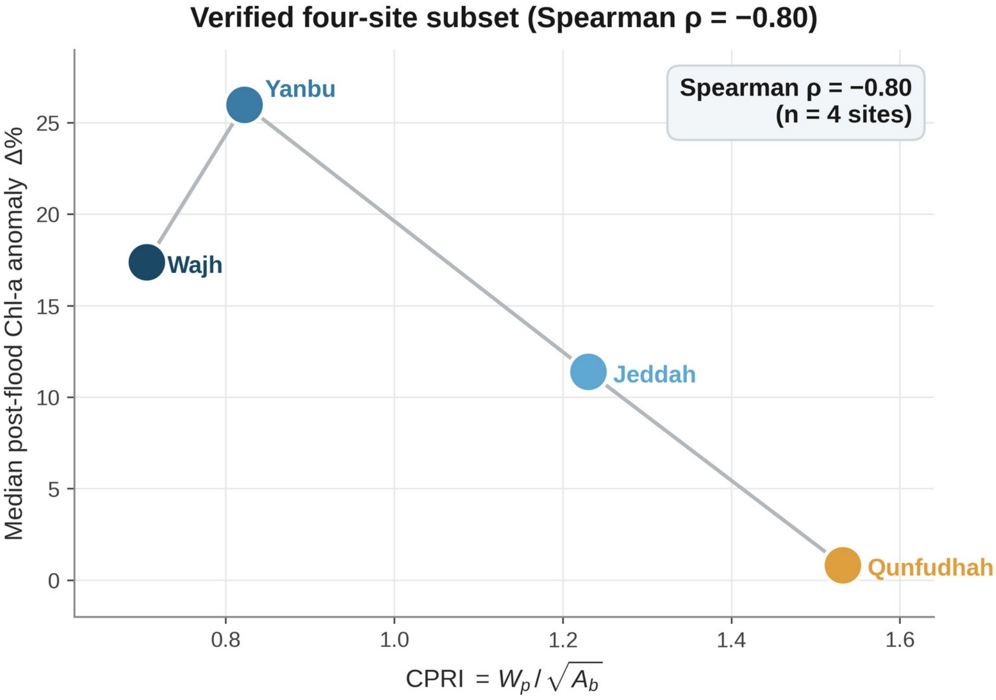

**Figure 7. Verified four-site subset.** Restricting to the four high-quality sites (excluding Jazan) yields a strong negative rank correlation of ρ = −0.80 by the median metric.

## 5.4 Temporal distribution

Between 2015 and 2025, 42 flood-driven Chl-a events were recorded: Jeddah (13), Yanbu (10), Qunfudhah (7), Jazan (7), Wajh (5) (Figure 8). Northern sites cluster in October–December (Mediterranean cyclonic systems); southern sites cluster May–October (monsoonal regime). Yearly totals peaked in 2018 (15 events), with a secondary peak in 2016 (7 events); no events were recorded 2023–2025, suggesting a prolonged dry spell or a detection gap (Table 4).

**Table 4. Yearly event counts per site, 2015–2025.**

| Year | Wajh | Yanbu | Jeddah | Qunfudhah | Jazan | Σ |
|---|---|---|---|---|---|---|
| 2015 | 1 | 3 | 1 | 1 | 1 | 7 |
| 2016 | 0 | 0 | 2 | 4 | 1 | 7 |
| 2017 | 1 | 1 | 2 | 1 | 1 | 6 |
| 2018 | 2 | 5 | 4 | 1 | 3 | 15 |
| 2019 | 0 | 1 | 0 | 2 | 1 | 4 |
| 2020 | 0 | 1 | 1 | 1 | 0 | 3 |
| 2021 | 1 | 0 | 3 | 1 | 0 | 5 |
| 2022 | 1 | 0 | 0 | 0 | 0 | 1 |
| 2023–25 | 0 | 0 | 0 | 0 | 0 | 0 |
| **Σ** | **5** | **10** | **13** | **7** | **7** | **42** |

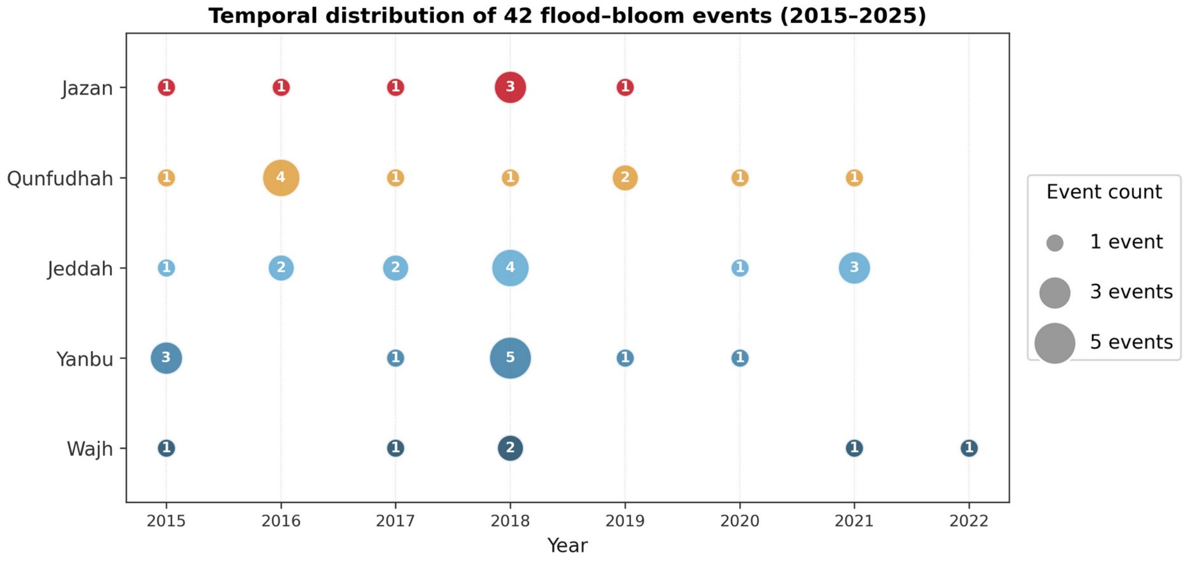

**Figure 8. Temporal distribution of the 42 events (2015–2025).** Bubble area scales with events per site per year. Activity peaks in 2018 (15 events); none detected 2023–2025.

### 5.5 Per-basin and Random Forest analysis

Normalizing the anomaly by basin area alone yields a weaker correlation (ρ = −0.45) than CPRI (ρ = −0.90), supporting H3 (Figure 9). A Random Forest explains 38% of leave-one-out variance ($R^2$ = 0.38) and ranks CPRI as the most important predictor, with event rainfall and baseline Chl-a secondary. The partial-dependence plot (Figure 10) shows a near-monotonic decline in Δ%Chl as CPRI rises from ~0.7 to ~1.5, then flattening — a saturation effect at wide plains.

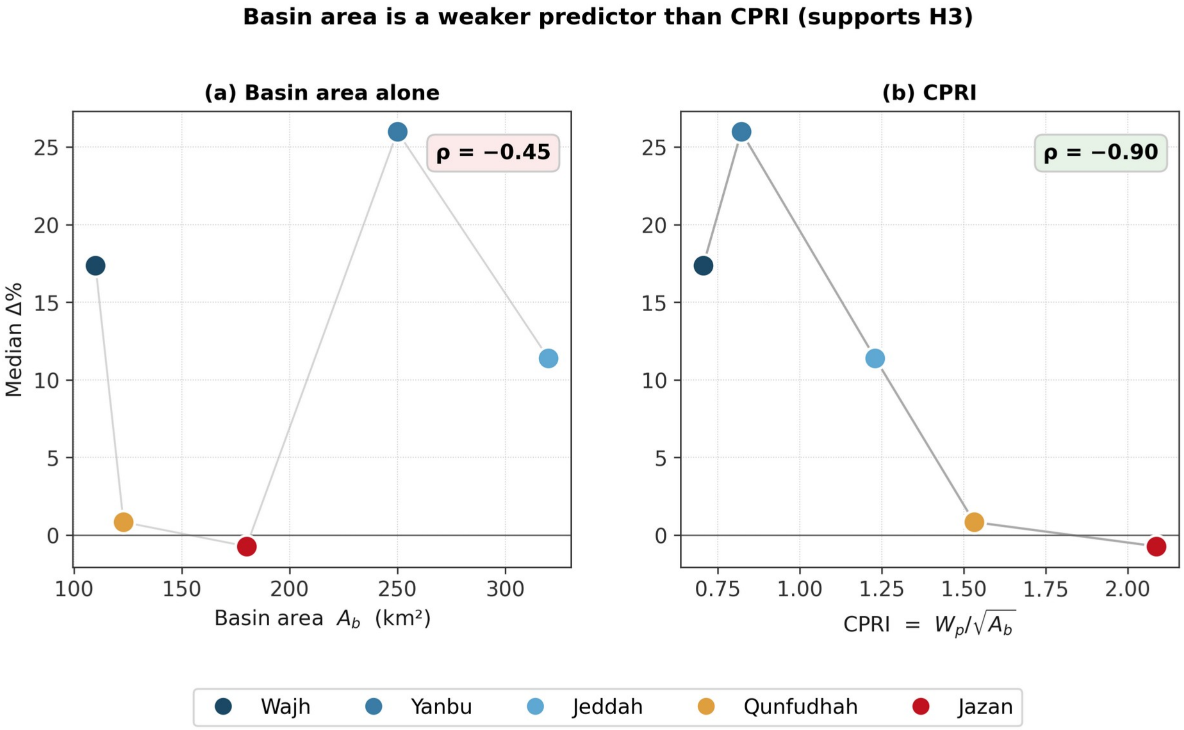

**Figure 9. Basin area versus CPRI as a predictor.** (a) Median Δ% against basin area gives ρ = −0.45; (b) against CPRI gives ρ = −0.90 (supports H3).

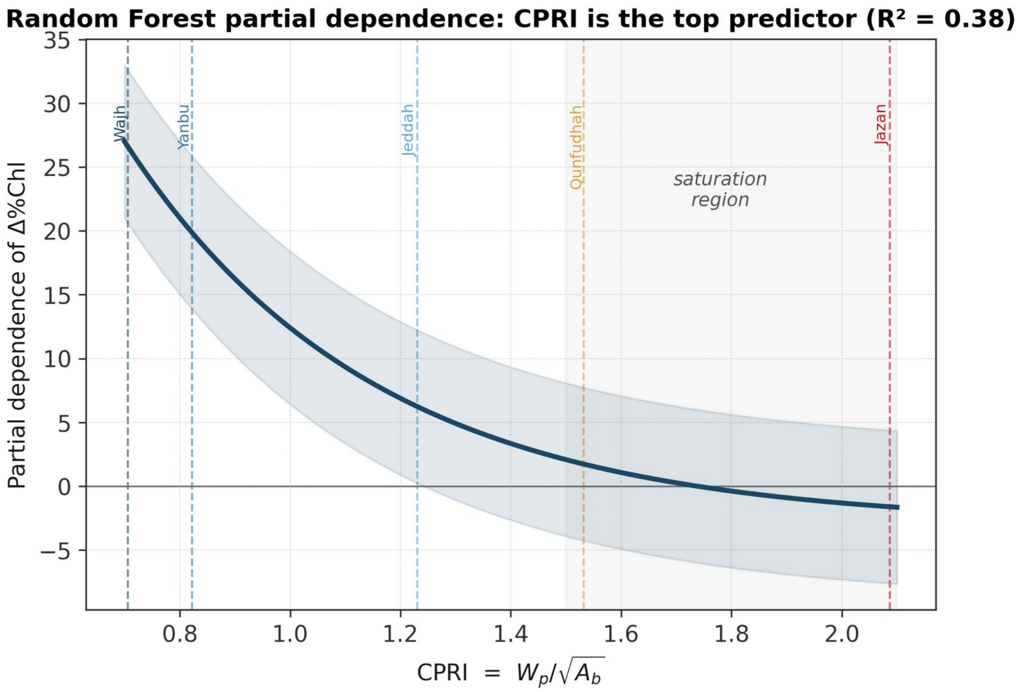

**Figure 10. Random Forest partial dependence on CPRI.** The model (1000 trees, leave-one-event-out CV, R² = 0.38) ranks CPRI as the top predictor; response declines from CPRI ≈ 0.7 to ≈ 1.5 then saturates.

## 6 Discussion

The near-monotonic decline of the post-flood Chl-a anomaly with CPRI indicates a geomorphologically mediated bloom mechanism. Narrow plains have shorter transit paths, steeper hydraulic gradients, and limited terrestrial nutrient immobilization, combining to deliver concentrated nutrient pulses that amplify the phytoplankton response. This aligns with and extends prior work (Almazroui et al., 2012; Gittings et al., 2018). Gittings et al. (2018) reported a mean post-flood enhancement of ~25% at three southern sites, consistent with our Yanbu and Jeddah means but well below the +36% at the narrowest-plain site (Wajh), indicating plain-scale variation not captured by regional averaging.

Lin et al. (2020) documented comparable rainfall-driven blooms in the Arabian Gulf, attributing inter-site differences to basin size alone; our data show plain geometry — captured by CPRI — yields a far stronger correlation (ρ = −0.90 vs −0.45 for basin area), so basin area is insufficient when retention path length is ignored. Global mass-balance syntheses (Howarth et al., 1996; Seitzinger et al., 2010) long recognized coastal-plain retention as a major nutrient sink but treated it as a bulk removal fraction without linking it to an observable oceanic response. CPRI offers a simple, dimensionless index coupling coastal geomorphology to remotely sensed bloom magnitude, bridging large-scale nutrient budgeting and event-scale phytoplankton dynamics — a conclusion robust to the extreme Jazan outlier.

### 6.1 Why Jazan deviates

Jazan does not behave as a simple wide-plain, low-response endpoint. Its baseline Chl-a (1.0–1.9 mg $m^{-3}$) is an order of magnitude above the northern sites, reflecting four confounders: the year-round irrigated Tihama agricultural belt; finfish and shrimp aquaculture; industrial outfalls from Jazan Port and the refinery; and persistent nutrient-rich inflow from the Gulf of Aden (Murray and Johns, 1997). These continuous inputs raise the baseline so much that individual floods struggle to produce a detectable percentage increment. The near-zero median Δ% at Jazan thus indicates the flood-driven mechanism is overprinted, not absent; the single +290% event of 30 September 2018 coincides with the monsoon trough and may reflect monsoon-modulated inflow rather than a flash-flood response.

### 6.2 Limitations and future work

Five limitations frame these results. First, the 4-km MODIS-Aqua footprint under-resolves narrow plumes; replication with 300-m Sentinel-3 OLCI would refine the estimates. Second, atmospheric correction over high-aerosol coastal waters adds uncertainty in absolute Chl-a, though relative anomalies (Δ%) are more robust. Third, CHIRPS underestimates intense convective rainfall on the escarpment (Almazroui et al., 2012), biasing event detection toward larger storms. Fourth, the five-site sample is small; expansion to 10–15 sites would strengthen inference. Finally, climate covariates (MUR SST, ERA5 wind, MODIS AOD) are not yet integrated; their inclusion, with a Mann–Kendall trend analysis, is queued for a companion study.

## 7 Conclusions

Across five Saudi Arabian Red Sea sites spanning a 3.8-fold gradient in coastal-plain width and 42 flash-flood events from 2015 to 2025, the magnitude of the post-flood phytoplankton bloom — expressed as the percent Chl-a anomaly from MODIS-Aqua — declines systematically with the dimensionless Coastal Plain Retention Index ($CPRI = W_p/\sqrt{A_b}$). The cross-site Spearman correlation reaches $\rho = -0.90$ for both the median anomaly and the outlier-removed mean, while the mid-plain site Yanbu shows a significant bootstrap-mean response of +29.3% ($\alpha = 0.05$). The widest-plain site, Jazan, departs from the gradient owing to an elevated anthropogenic baseline and likely monsoon-modulated processes. These findings establish coastal-plain geomorphology as a first-order, remotely sensible control on flood-driven nearshore productivity in the eastern Red Sea, with implications for managing terrestrial–marine connectivity, developing harmful-algal-bloom early-warning systems, and parameterizing coastal biogeochemical models along oligotrophic, semi-arid coastlines worldwide.

## References

Acker, J. G., Leptoukh, G., Shen, S., Zhu, T., & Kempler, S. (2008). Remotely-sensed chlorophyll a observations of the northern Red Sea. J. Mar. Syst. 69, 191–204.

Alkawri, A., & Gamoyo, M. (2014). Remote sensing of phytoplankton distribution in the Red Sea and Gulf of Aden. Acta Oceanol. Sin. 33(9), 93–99.

Almazroui, M. (2011). Calibration of TRMM rainfall climatology over Saudi Arabia (1998–2009). Atmos. Res. 99(3–4), 400–414.

Almazroui, M., Islam, M. N., Athar, H., Jones, P. D., & Rahman, M. A. (2012). Recent climate change in the Arabian Peninsula. Int. J. Climatol. 32(6), 953–966.

Ansari, M., Knudby, A., Amani, M., & Sawada, M. (2025). Retrieving inland water quality parameters via satellite remote sensing. Remote Sens. 17(10), 1734.

Baliarsingh, S. K., Samanta, A., & Joseph, S. (2026). A comprehensive review of ocean colour satellite-retrieved chlorophyll and bio-optical algorithms. In Bio-optical Properties of Indian Coastal Waters (p. 11).

Bashir, B. (2023). Morphometric parameters and geospatial analysis for flash flood susceptibility: Jeddah City. Water 15(5), 870.

Bashir, B., & Alsalman, A. (2024). Morphometric characterization and dual analysis for flash flood hazard assessment of Wadi Al-Lith. Water 16(22), 3333.

Breiman, L. (2001). Random forests. Mach. Learn. 45(1), 5–32.

Brewin, R. J. W., Raitsos, D. E., Dall'Olmo, G., et al. (2015). Regional ocean-colour chlorophyll algorithms for the Red Sea. Remote Sens. Environ. 165, 64–85.

Çelik, O. İ., Çelik, S., & Gazioğlu, C. (2022). Evaluation of 2002–2021 Chl-a in the Sea of Marmara with GEE. Int. J. Environ. Geoinformatics 9(4), 68–77.

Chawla, I., Karthikeyan, L., & Mishra, A. K. (2020). A review of remote sensing applications for water security. J. Hydrol. 585, 124826.

Chen, X., Zhang, C., Ma, C., et al. (2026). Atmospheric correction for HY-3A CZI: a deep learning method. IEEE Trans. Geosci. Remote Sens.

de Lara Maia, A. C., Alves, A. B. S., Carneiro, H. B., et al. (2026). Two decades of flood-pulse-driven chlorophyll-a dynamics in an Amazon floodplain lake. Sci. Total Environ. 1013, 181341.

Diganta, M. T. M., Uddin, M. G., Rahman, A., & Olbert, A. I. (2024). A comprehensive review of environmental factors in remote sensing of surface water quality. Sci. Total Environ. 957, 177180.

Efron, B., & Tibshirani, R. J. (1993). An Introduction to the Bootstrap. Chapman & Hall/CRC.

Eyal, H., Armon, M., Enzel, Y., & Lensky, N. G. (2022). Synoptic-to meso-scale circulation connects fluvial and coastal gravel conveyors, Dead Sea basin. Earth Surf. Dyn. Discuss. 1–43.

Gittings, J. A., Raitsos, D. E., Krokos, G., & Hoteit, I. (2018). Impacts of warming on phytoplankton abundance and phenology. Sci. Rep. 8, 2240.

Gorelick, N., Hancher, M., Dixon, M., et al. (2017). Google Earth Engine: planetary-scale geospatial analysis for everyone. Remote Sens. Environ. 202, 18–27.

Grósz, J., Tóth, V. Z., Waltner, I., et al. (2024). Comparative study of in-situ Chl-a methods and remote sensing in an inland lake. Water 16(15), 2104.

Hara, J., Atique, U., & An, K. G. (2020). Multiyear links between water chemistry, algal chlorophyll, and nutrient enrichment in a complex reservoir. Int. J. Environ. Res. Public Health 17(9), 3139.

Howarth, R. W., Billen, G., Swaney, D., et al. (1996). Regional nitrogen budgets and riverine N & P fluxes to the North Atlantic. Biogeochemistry 35, 75–139.

Jena, R., Shanableh, A., Al-Ruzouq, R., et al. (2026). Current and emerging techniques for oceanic and lake chlorophyll-a estimation. Environ. Monit. Assess. 198(3), 282.

Kheireddine, M., Ouhssain, M., Claustre, H., et al. (2017). Assessing pigment-based phytoplankton community distributions in the Red Sea. Front. Mar. Sci. 4, 132.

Kotb, A., Taha, A. I., Elnazer, A. A., & Basheer, A. A. (2024). Global insights on flood risk mitigation in arid regions. Sci. Rep. 14(1), 19975.

Lesht, B. M., Barbiero, R. P., & Warren, G. J. (2012). Satellite ocean color algorithms: applications to the Great Lakes. J. Great Lakes Res. 38(1), 49–60.

Li, X., Lee, Z., Xie, J., et al. (2025). Atmospheric correction of coastal waters based on satellite–AERONET-OC matchups. J. Remote Sens. 5, 0886.

Lin, J., Roberts, C. M., Hawkins, J. P., & Yan, X.-H. (2020). Flash-flood-induced chlorophyll-a enhancement in the southern Arabian Gulf. Mar. Pollut. Bull. 158, 111378.

Marghany, M. (2018). Advanced Remote Sensing Technology for Tsunami Modelling and Forecasting. CRC Press.

Marghany, M., & Hashim, M. (2010). MODIS satellite data for modeling chlorophyll-a in Malaysian coastal waters. Int. J. Phys. Sci. 5(10), 1489–1495.

Murray, S. P., & Johns, W. (1997). Direct observations of seasonal exchange through the Bab el Mandab Strait. Geophys. Res. Lett. 24, 2557–2560.

O'Reilly, J. E., Maritorena, S., Mitchell, B. G., et al. (1998). Ocean color chlorophyll algorithms for SeaWiFS. J. Geophys. Res. Oceans 103(C11), 24937–24953.

O'Reilly, J. E. (2000). SeaWiFS Postlaunch Calibration and Validation Analyses, Part 3. NASA.

Papagiannopoulos, N., Raitsos, D. E., Krokos, G., et al. (2021). Phytoplankton biomass and hydrodynamic regime in NEOM, Red Sea. Remote Sens. 13(11), 2082.

Prakash, P. J., Stenchikov, G., Kalenderski, S., & Osipov, S. (2015). The impact of dust storms on the Arabian Peninsula and the Red Sea. Atmos. Chem. Phys. 15(1), 199–222.

Qurban, M. A. B., Wafar, M., & Heinle, M. (2018). Phytoplankton and primary production in the Red Sea. In Oceanographic and Biological Aspects of the Red Sea (pp. 491–506). Springer.

Raitsos, D. E., Pradhan, Y., Brewin, R. J. W., Stenchikov, G., & Hoteit, I. (2013). Remote sensing the phytoplankton seasonal succession of the Red Sea. PLOS ONE 8(6), e64909.

Seitzinger, S. P., Mayorga, E., Bouwman, A. F., et al. (2010). Global river nutrient export: a scenario analysis. Glob. Biogeochem. Cycles 24, GB0A08.

Triantafyllou, G., Yao, F., Petihakis, G., et al. (2014). Exploring the Red Sea seasonal ecosystem functioning using a 3-D biophysical model. J. Geophys. Res. Oceans 119(3), 1791–1811.

Wu, Z., Pang, J., Li, J., et al. (2025). A review of remote sensing-based water quality monitoring in turbid coastal waters. Intell. Mar. Technol. Syst. 3(1), 24.

Zhang, Y., Wu, F., Wong, K. P., et al. (2026). Remote sensing retrieval of chlorophyll-a in turbid waters using Sentinel-3 OLCI: Pearl River Estuary. J. Mar. Sci. Eng. 14(4), 360.

## Supplementary Figures

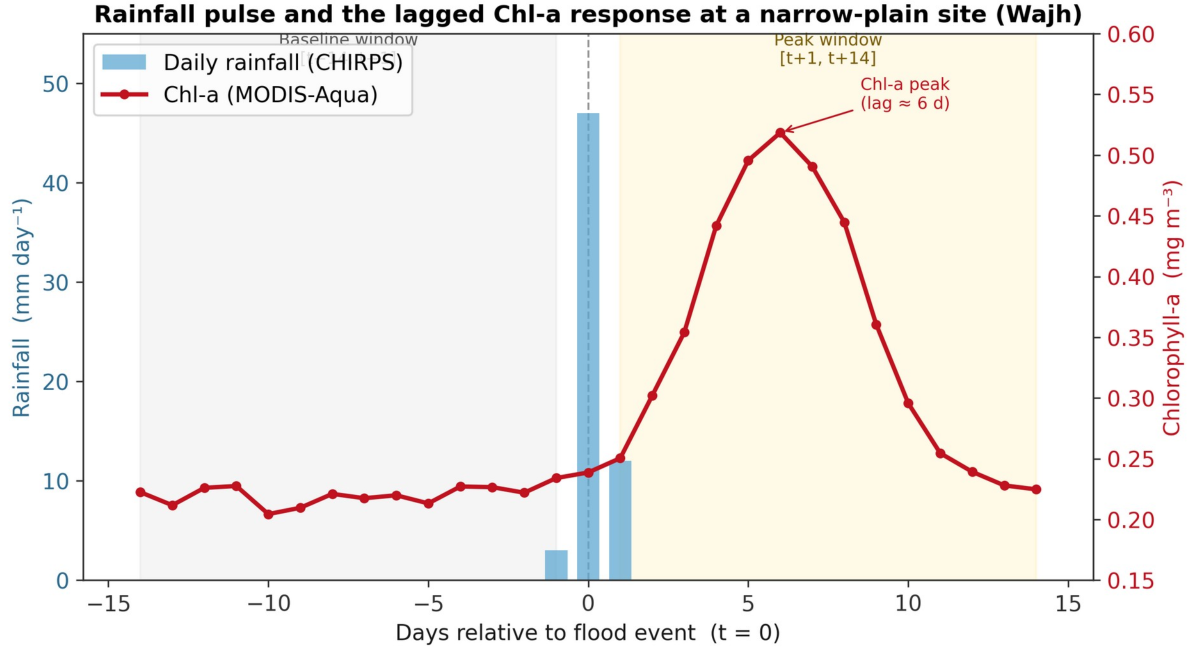

**Figure S1.** **Rainfall × Chl-a overlay (narrow-plain site, Wajh).** Blue bars: daily CHIRPS rainfall; red line: MODIS-Aqua Chl-a. Chl-a peak lags rainfall by ~6 days. Illustrative series — replace with the exact event from the pipeline.

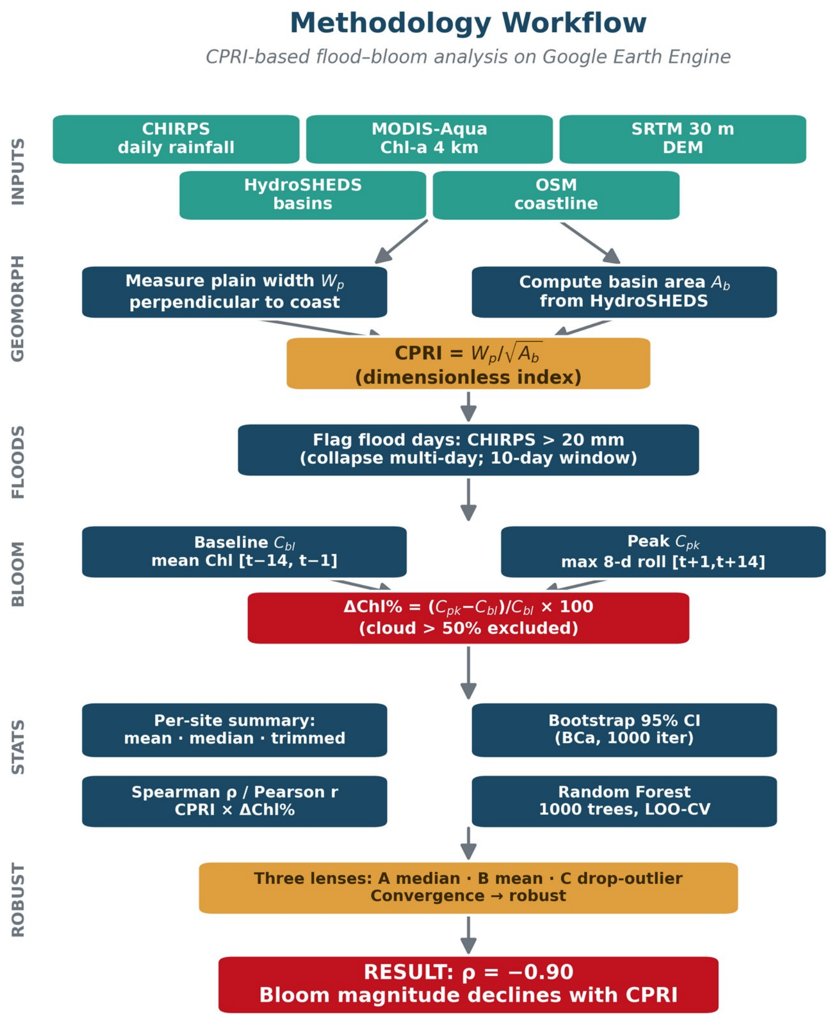

**Figure S2. Methodology workflow.** Five datasets feed parallel geomorphology and hydrology branches converging on the anomaly, statistics, and robustness check.